


Cite this: *RSC Adv.*, 2020, 10, 5220

Self-assembly and multifunctionality of peptide organogels: oil spill recovery, dye absorption and synthesis of conducting biomaterials†

Monikha Chetia,‡ Swapna Debnath,‡ Sumit Chowdhury and Sunanda Chatterjee *

The self-assembly of a series of low molecular weight gelator dipeptides containing *para* amino benzoic acid has been studied in mechanistic detail. All four dipeptides form phase selective, thermoreversible, rigid gels in a large range of organic solvents and fuels such as petrol, diesel, and kerosene. The mechanism of self-assembly has been dissected in detail using several experimental techniques. Self-assembly is driven mainly by aromatic and hydrophobic interactions. Hydrogen bonding groups, though present, seem to make a trivial contribution towards the self-assembly process. Phase selective gelation abilities in fuels in the presence of acidic, basic and saline conditions, together with the easy recovery of fuels from the organogels, render the peptides potential candidates for addressing oil-spill recovery. Being electron rich systems, these organogelators can absorb cationic dyes with >90% efficiency from wastewater. Finally, conducting biomaterials have been synthesized by the insertion of reduced graphene oxide into the organogels. Such small peptide based gelator molecules, being economically viable and easy to prepare, in addition to being multifunctional, are a hot area of research in the field of materials chemistry.

Received 11th December 2019
Accepted 19th January 2020

DOI: 10.1039/c9ra10395c

rsc.li/rsc-advances

Introduction

Low molecular weight supramolecular gels (LMWGs) are an important class of materials that can encapsulate large amounts of solvents in mesh-like entangled structures that are formed *via* the ordered hierarchical arrangement of individual molecules.^{1–4} These assemblies are driven by non-covalent forces such as hydrogen bonding, π - π interactions, hydrophobic interactions, van der Waals forces, charge transfer interactions, *etc.*,^{5–9} and can be controlled by various stimuli such as concentration, pH, UV radiation, temperature, solvent polarity and by salts.^{10–24} Various small molecules such as amides, peptides, ureas, peptoids, nucleobases, *etc.* have shown spectacular abilities to self-assemble. Supramolecular gels have been used in various applications such as in water purification, through the removal of organic dyes, oils and metal ions;^{25–38} as templates for nanoparticle fabrication;^{39–44} and in cosmetics, catalysts,^{45,46} dye sensitized solar cells,⁴⁷ drug delivery systems,^{48–54} *etc.* Although the self-assembly of peptides was achieved serendipitously previously, extensive research over the last couple of decades has established that, by proper choice of

the individual building blocks that are capable of promoting various non-covalent interactions, smart molecules with predictable and tunable self-assembling properties can be designed. However, even now the design of LMWGs is an important field of research due to their reduced expenditure, easy synthesis, biocompatibility and multifunctionality.

Water pollution is one of the fundamental environmental problems faced by humanity at present. Marine oil spills due to the leakage of crude oil and petroleum products (*i.e.* fuels) are a major source of water pollution that creates a great environmental hazard for marine ecosystems.⁵⁵ Different methods such as bioremediation,^{56,57} dispersants,⁵⁸ solidifiers,^{59–61} sorbents^{62–64} and skimmers^{65–67} have been developed to tackle the problem. However, each of these approaches have their own shortcomings.⁶⁸ Hydro/organogel materials have also been used in the recovery of oil spills.^{26,68–71} Another critical source of water pollution is the organic dyes that are routinely used in several industries.⁷² Dye effluents and their degradation products are carcinogenic, and have a negative impact on the reproductive and immune systems.^{73–77} Conventional methods of treating dye effluents such as incineration, biological treatment, absorption upon solid matrices such as activated carbon, chemical precipitation, electrochemical techniques, ion exchange, and others, have their own limitations due to their low sensitivity, incomplete removal, high energy requirements, and production of toxic sludge.⁷⁸ Hydro/organogel-based soft materials^{28–38} offer an appealing alternative for the removal of dyes from contaminated water, due to their high water permeability, large surface area for

Department of Chemistry, Indian Institute of Technology, Guwahati, Guwahati, Assam, India, 781039. E-mail: sunanda.c@iitg.ac.in; Tel: +91-361-2583310

† Electronic supplementary information (ESI) available. CCDC 1961450 and 1961451. For ESI and crystallographic data in CIF or other electronic format see DOI: 10.1039/c9ra10395c

‡ These authors have contributed equally.



adsorption and simplicity of use, along with their reusability and good biodegradability.

The supramolecular assembly of bioconjugates appended to optoelectronically active π -conjugated chromophores in organic solvents has already been reported.^{79–84} Hybrid materials using graphene and its derivatives with inorganic/polymeric materials are highly conducting and have been used in interesting applications including renewable energy conversion/storage devices, supercapacitors, electroresponsive systems, electrocatalysis, optoelectronic devices, electromagnetic interference shielding *etc.*^{85–96} In a number of studies, graphene and its derivatives have also been incorporated into peptide organogels. Peptide-based hybrid materials become moderately conducting in nature upon insertion of graphene or its derivatives.^{97–100}

In this study, four dipeptides, **P1–P4**, which are rich in aromatic moieties were synthesized in order to study their self-assembly and to generate materials with multiple applications. The building blocks of **P1–P4** were chosen so that their self-assembly would be guided by aromatic and hydrophobic interactions. The mechanism of self-assembly of **P1–P4** was established using various spectroscopic and microscopic experiments. Interestingly, all the peptides were capable of forming gels in a variety of organic solvents and in fuels such as petrol, diesel and kerosene, and this made them ideal materials to be used for oil spill recovery. All the organogels studied here were excellent adsorbents for cationic dyes. RGO was incorporated into the peptide organogels to generate conducting biomaterials. Generating environmentally friendly materials that have multiple applications, using directed self-assembly methods, is of considerable interest and was the main focus of our study.

Materials and methods

Materials

All amino acids, L-Phe, L-Trp, PABA, L-Phe, L-HomoPhe, all solvents, di-*t*-butyl dicarbonate, *N,N'*-dicyclohexylcarbodiimide (DCC), sodium hydroxide, 1-hydroxybenzotriazole (HOBt), and thionyl chloride were purchased from Spectrochem, Merck and Rankem. CDCl_3 and DMSO-d_6 solvents were obtained from Sigma Aldrich. The dyes crystal violet (CV) and rhodamine B (RB) were purchased from Spectrochem. Fuels such as kerosene, diesel and petrol were obtained from Bharat Petroleum Gas Station. Graphite powder was purchased from Asbury Carbons.

Methods

Synthesis of peptides. All peptides were synthesized by a racemization-free, fragment condensation technique based on traditional solution phase methodology. The N-termini of the amino acids were protected by Boc groups using $(\text{Boc})_2\text{O}$, while the C-termini were protected as methyl esters. Peptide couplings were carried out using DCC and HOBt as coupling reagents. All compounds were purified by column chromatography using silica gel (100–200 mesh size) as the stationary

phase and hexane/ethyl acetate as the eluent. Finally, dipeptides were characterized by analytical HPLC (Fig. S1–S4†), mass spectrometry (Fig. S5–S8†) and ^1H NMR spectroscopy (400 MHz and 600 MHz) (Fig. S9–S12†).

Yield: **P1**, 78%; **P2**, 80%; **P3**, 82%; **P4**, 86%.

All peptides were characterized using HPLC (Fig. S1–S4†), ESI-MS (Fig. S5–S8†) and ^1H NMR (Fig. S9–S12†).

ESI-MS. ESI-MS of **P1**. Mass calc. for **P1**: $(\text{M} + \text{H})^+ = 438.208$ Da; mass obs.: $(\text{M} + \text{H})^+ = 438.2092$ Da.

ESI-MS of **P2**. Mass calc. for **P2**: $(\text{M} + \text{H})^+ = 413.208$ Da; mass obs.: $(\text{M} + \text{H})^+ = 413.2020$ Da.

ESI-MS of **P3**. Mass calc. for **P3**: $(\text{M} + \text{H})^+ = 385.178$ Da; mass obs.: $(\text{M} + \text{H})^+ = 385.1934$ Da.

ESI-MS of **P4**. Mass calc. for **P4**: $(\text{M} + \text{H})^+ = 399.188$ Da; mass obs.: $(\text{M} + \text{H})^+ = 399.1927$ Da.

^1H NMR. **P1** (Fig. S9†): ^1H NMR (400 MHz, DMSO-d_6) δ 10.82 (s, 1H, NH of indole ring), 10.40 (s, 1H, NH of backbone), 7.92 (d, $J = 8.5$ Hz, 2H, aromatic ring Hs), 7.75 (d, $J = 8.6$ Hz, 2H, aromatic ring Hs), 7.65 (d, $J = 7.9$ Hz, 1H, aromatic ring H), 7.32 (d, $J = 8.1$ Hz, 1H, NH of Boc group), 7.18 (s, 1H, H of aromatic ring), 7.05 (t, $J = 7.7$ Hz, 2H, aromatic ring Hs), 6.97 (t, $J = 7.4$ Hz, 1H, H of aromatic ring), 4.39 (d, $J = 6.7$ Hz, 1H, H of α -CH), 3.82 (s, 3H, Hs of $-\text{CH}_3$ group), 3.12 (dd, $J = 14.6$, 5.3 Hz, 1H, H of β - CH_2), 3.00 (dd, $J = 14.5$, 9.0 Hz, 1H, H of β - CH_2), 1.33 (s, 9H, Hs of Boc group).

P2 (Fig. S10†): ^1H NMR (600 MHz, DMSO-d_6) δ 10.36 (s, 1H, NH of backbone), 7.93–7.89 (m, 2H, Hs of aromatic ring), 7.74 (d, $J = 8.8$ Hz, 2H, Hs of aromatic ring), 7.32 (d, $J = 7.6$ Hz, 1H, NH of Boc group), 7.27 (t, $J = 7.5$ Hz, 2H, Hs of aromatic ring), 7.24–7.19 (m, 2H, Hs of aromatic ring), 7.19–7.15 (m, 1H, H of aromatic ring), 4.10 (ddd, $J = 9.5$, 7.5, 4.7 Hz, 1H, H of α -CH group), 3.82 (s, 3H, Hs of $-\text{CH}_3$ group), 2.71 (ddd, $J = 13.3$, 10.8, 5.0 Hz, 1H, H of β - CH_2 group), 2.58 (ddd, $J = 13.5$, 10.8, 5.9 Hz, 1H, H of β - CH_2), 1.97–1.83 (m, 2H, Hs of γ - CH_2 group), 1.40 (s, 9H, Hs of Boc group).

P3 (Fig. S11†): ^1H NMR (400 MHz, DMSO-d_6) δ 10.57 (s, 1H, H of backbone NH), 7.93–7.88 (m, 2H, Hs of aromatic ring), 7.74–7.68 (m, 2H, Hs of aromatic ring), 7.59 (d, $J = 8.1$ Hz, 1H, NH of Boc group), 7.52–7.47 (m, 2H, Hs of aromatic ring), 7.38–7.27 (m, 3H, Hs of aromatic ring), 5.36 (d, $J = 8.1$ Hz, 1H, H of α -CH), 3.81 (s, 3H, Hs of $-\text{CH}_3$), 1.39 (s, 9H, Hs of Boc group).

P4 (Fig. S12†): ^1H NMR (400 MHz, DMSO-d_6) δ 10.39 (s, 1H, NH of backbone), 7.96–7.90 (m, 2H, Hs of aromatic ring), 7.77–7.69 (m, 2H, Hs of aromatic ring), 7.29 (dt, $J = 14.8$, 7.5 Hz, 4H, Hs of aromatic ring and NH of Boc group), 7.20 (d, $J = 7.7$ Hz, 2H, Hs of aromatic ring), 4.44–4.16 (m, 1H, H of α -CH), 3.82 (s, 3H, Hs of $-\text{CH}_3$ group), 2.99 (dd, $J = 13.7$, 4.7 Hz, 1H, H of β - CH_2), 2.84 (dd, $J = 13.7$, 10.1 Hz, 1H, H of β - CH_2), 1.32 (s, 9H, Hs of Boc group).

Gelation. In order to check the ability of **P1–P4** to form gels in different solvents, weighed amount of the purified compounds (**P1–P4**) were taken in micro centrifuge tubes and 500 μL of different solvents were added to them. The samples were heated in a heating block at temperatures ranging from 60–100 $^\circ\text{C}$ and then they were subsequently cooled to room temperature. Gels were formed within 10–15 minutes that was stable to inversion of the micro centrifuge tube.



To make the RGO incorporated **P1** organogel (RGO-**P1**), the freshly prepared RGO (1 mg, 0.2 wt%) was added to 500 μL 1,2-DCB solution of peptide **P1** at its MGC. The mixture was sonicated until a homogeneous suspension of RGO in the peptide was obtained. This was further heated at 100 $^{\circ}\text{C}$ for 15 min, followed by vortexing for 10 s. Upon cooling the mixture, a black colored organogel was formed within a further 5–10 min. Hybrid organogels were formed by varying the amount of RGO.

Determination of the gel-to-sol transition temperature. The gel-to-sol transition temperatures (T_{gel}) of the organogels from single peptides and the RGO-peptide hybrid organogel were determined by placing the vials containing the gels in an oil bath and increasing the temperature of the bath at a rate of 1 $^{\circ}\text{C min}^{-1}$. The temperature was monitored using a thermometer. The T_{gel} value was defined as the temperature at which the gel melted and started to flow.

Phase selective gelation. Peptides **P1–P4** at their MGC were added to mixtures of 500 μL each of organic and aqueous solvents. The mixture was vortexed for 2 minutes to yield a homogeneous suspension, heated at 60–100 $^{\circ}\text{C}$ and subsequently cooled. Gels were selectively formed from the organic solvents within 10–15 min.

Rheology. The viscoelastic properties of the self-assembled and RGO incorporated hybrid organogels were determined by rheology studies using an Anton Paar MCR102 Rheometer equipped with a 20 mm parallel-plate measuring system at 25 $^{\circ}\text{C}$. 1.0 w/v% pristine organogels of **P1–P4** in 1,2-DCB and 1 wt% RGO incorporated in RGO-**P1** were used for the study. A strain sweep test was performed over a range from 0.1–100% strain at a fixed oscillating frequency of 1 rad s^{-1} . Furthermore, the mechanical strength of the organogels was determined from the oscillatory test, *i.e.* the frequency sweep (with the frequency ranging from 1–100), and this was carried out under a fixed strain. Rheological experiments measure two parameters: storage modulus (G') and loss modulus (G''). A defining measure of the gelation process is obtaining a higher value of G' than G'' , which are essentially independent of frequency.

FESEM. The field emission scanning electron microscope (FESEM) images reported in this study were obtained on an FESEM Sigma Zeiss microscope. A drop of the solution of **P1–P4** in 1,2-DCB was cast on a silicon wafer and was allowed to dry for a few hours under vacuum before imaging. To study the morphology of the pristine organogels **P1–P4** and the hybrid gel RGO-**P1**, small pieces of the organogel were cast on the silicon wafer and allowed to dry under vacuum before imaging.

FT-IR. Fourier-transform infrared (FT-IR) spectroscopy measurements were recorded on a Spectrum Two PerkinElmer FT-IR Instrument using KBr pellets. Measurements were performed on both powdered samples and on xerogels (obtained from organogels in 1,2-DCB) for **P1–P4**. Lyophilized peptides that were obtained post-purification were used as powdered samples. Measurements were also performed on xerogels of **P1** (obtained from the organogel in kerosene) and RGO-**P1** (obtained from the organogel in 1,2-DCB). The xerogels were prepared by keeping the organogels in a desiccator under vacuum conditions. After 3–4 days it visibly became a white, dry

and solid mass. This solid mass was used for making KBr pellets in the FT-IR analysis.

NMR. Nuclear magnetic resonance (NMR) experiments were performed on a 600 MHz and a 400 MHz Bruker NMR spectrometer. ^1H NMR experiments were performed in DMSO-d_6 for the routine characterization of the molecule. Concentration dependent ^1H NMR (5 mM, 6.86 mM (MGC), 9 mM and 13 mM for **P1**; 2 mM, 3 mM, 4.8 mM (MGC) and 7 mM for **P2**) was recorded for the peptides **P1** and **P2** in CDCl_3 at ambient temperature. DMSO titrations of **P1** and **P2** were performed by the addition of increasing concentrations (0.5% to 10%) of DMSO-d_6 in CDCl_3 at ambient temperature.

Fluorescence. To gain insight into the role of aromatic π - π stacking in the self-assembly of **P1**, a concentration dependent fluorescence experiment was performed by monitoring the intrinsic fluorescence of the amino acid Trp on a Fluoromax-4 spectrophotometer. Samples of different concentrations of **P1** were prepared in THF and their fluorescence emission was monitored, keeping the fluorescence excitation wavelength fixed at 280 nm.

PXRD. Wide angle X-ray diffraction analysis was carried out on a Bruker D2 Phaser X-ray diffractometer ($\text{Cu-K}\alpha$ radiation, $\lambda = 1.5406 \text{ \AA}$) and using a Rigaku Smartlab X-ray diffractometer ($\text{Cu-K}\alpha$ radiation, $\lambda = 1.540 \text{ \AA}$) for both the powdered samples (**P1–P4**) (as obtained post lyophilization) and for the xerogels obtained from drying the organogels (described above) of (a) individual peptides (**P1–P4**) grown from 1,2-DCB, (b) **P1** in kerosene and (c) the RGO-**P1** hybrid organogel obtained from 1,2-DCB. Powder X-ray diffraction (PXRD) measurements were carried out on the GO and RGO synthesized for characterization of the materials.

Crystallization and X-ray crystallography. Single crystals were obtained from peptides **P2** and **P4** in $\text{MeOH-H}_2\text{O}$ solvent systems. Intensity data was collected with $\text{Mo-K}\alpha$ radiation ($\lambda = 0.71073 \text{ \AA}$) by a Bruker APEX-2 CCD diffractometer. Data was processed using the Bruker SAINT package. The structure solution and refinement were performed by SHELX2016.

FETEM and EDX analysis. The synthesized GO and RGO were characterized using field emission transmission electron microscopy (FETEM). The samples were prepared by casting the suspensions containing GO and RGO on the TEM grid and letting them dry for a couple of days under vacuum. FETEM was performed using a JEOL (JEM-2100F) transmission electron microscope with an operating voltage of 200 kV. Energy-dispersive X-ray (EDX) spectroscopic analysis was performed to determine the percentages of carbon and oxygen in the GO and RGO samples.

Raman analysis. Raman analysis of GO and RGO was carried out using a laser micro-Raman (Horiba Jobin Yvon LabRam HR) with 514 nm laser excitation.

Dye absorption studies. An aqueous solution of dye was added to the preformed gels obtained from the self-assembly of the individual peptides **P1–P4**, and this was allowed to stand for 24 hours at RT, after which the amount of unabsorbed dye in the supernatant was checked by monitoring the UV of the supernatant aqueous solution and calculating the concentration from a standard curve of the dye. The amount of dye loaded



in the gel and the dye loading efficiency were then calculated as follows:

$$\text{Dye loaded} = \text{initial dye} - \text{unabsorbed dye},$$

$$\text{loading efficiency} = (\text{dye loaded}/\text{initial dye}) \times 100$$

Recyclability of the organogels for dye absorption. To the dye absorbed organogels, diethyl ether was added and left for 24 hours. The dye was released into the ether medium and the gel became colorless again. The ether layer was removed and after another round of ether washing, the gel was reused for the second cycle of dye absorption studies. Such studies were carried out for 3 subsequent cycles and the efficiency of the dye absorption was estimated in each cycle.

Conductivity determination of the RGO-peptide hybrid organogels. Two copper wires were inserted into the RGO-P1 (with different amounts of RGO) hybrid organogel and were connected to the sourcemeter (Keithley 2450 model). A potential of -1 to $+1$ was applied, and the conductivity measurements (*i.e.* current-voltage (I - V) characteristics) were recorded.

Results and discussion

We synthesized four dipeptides, Boc-Trp-PABA-OMe (**P1**), Boc-homoPhe-PABA-OMe (**P2**), Boc-Phg-PABA-OMe (**P3**) and Boc-Phe-PABA-OMe (**P4**) (Fig. 1), using a standard solution based peptide synthesis strategy, purified them using column chromatography and characterized them using analytical HPLC, ^1H NMR and ESI-MS (Fig. S1–S12†). All four dipeptides were terminally protected and contained an aromatic delta amino acid residue, PABA. The second amino acid residue (Trp, Homo-Phe, Phg or Phe) was aromatic in nature. The design of the

building blocks intended to facilitate self-assembly using aromatic interactions and hydrophobic interactions. Homologs of Phe, namely Phg and Homo-Phe, were used to understand the role of the length of the side chain on the assembly of the peptides.

All of the dipeptides readily formed phase selective, thermoreversible gels in various organic solvents such as chloroform, THF, 1,2-dichlorobenzene, *etc.* (Fig. 1 and Table S1†) and in fuels such as kerosene, diesel and petrol, upon heating and subsequent cooling. The minimum gelation concentration of the peptides depended on the solvents, but it was generally between 0.2–0.4 w/v% (Table S1†). The thermal stability of the peptides was studied from the T_{gel} value, which was in the range of 30–80 °C. As the gels were translucent and were most thermostable in 1,2-DCB, further characterization of the organogels was carried out in this solvent.

The self-assembled morphologies of **P1–P4** in 1,2-DCB in both solution and gel states were studied using Field Emission Scanning Microscopy (FESEM) (Fig. 2 and S13†). It was clear that the morphology of **P1** in solution (Fig. S13†) and in the gel state (Fig. 2) were different. The morphology of **P1** was nano fibrous in the solution state, while it appeared as a densely packed continuous matrix in the gel state. The morphologies of the peptides **P2** and **P3** in solution and in the gel state were the same, but with slight variations. Peptide **P4** formed a fibrous entangled morphology both in solution and in the gel state, with a denser mesh in the latter. The subtle differences in the morphologies of **P1–P4** can be attributed to the varying chains of the amino acids present in them.

Rheology

The mechanical strength and the stability of the organogels derived from self-assembly of the individual peptides were

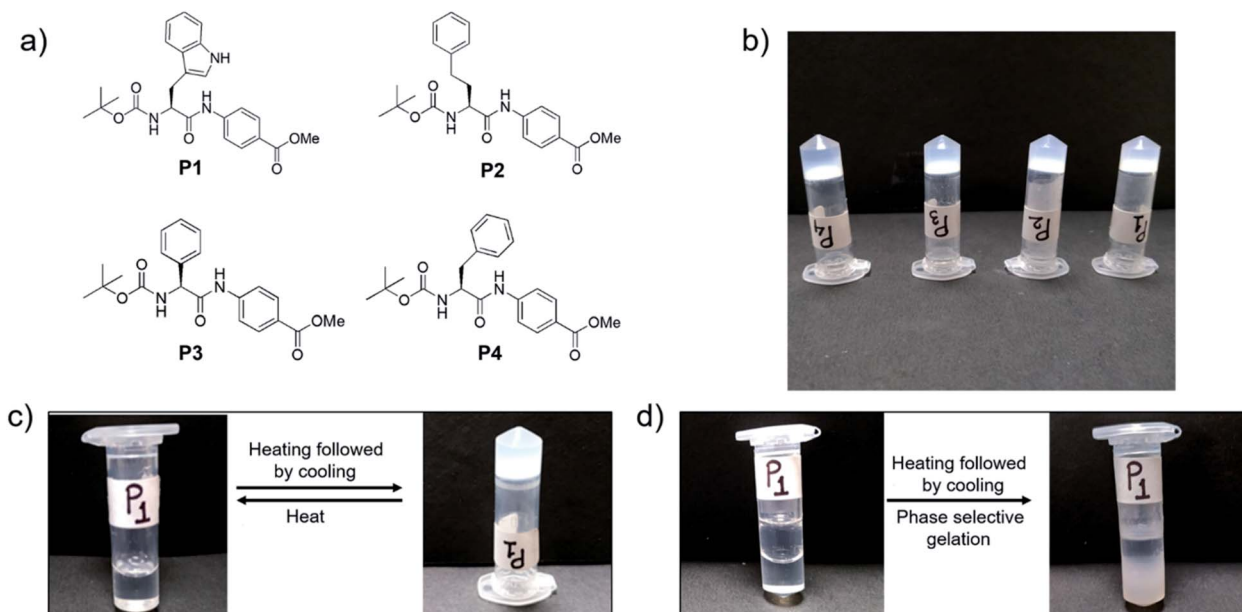


Fig. 1 (a) Chemical structures of LMWG **P1–P4**, (b) gels formed in 1,2-DCB by **P1–P4** (c) thermoreversibility of the organogel formed by **P1** in 1,2-DCB and (d) phase selective gelation of **P1** in 1,2-DCB in the presence of water.

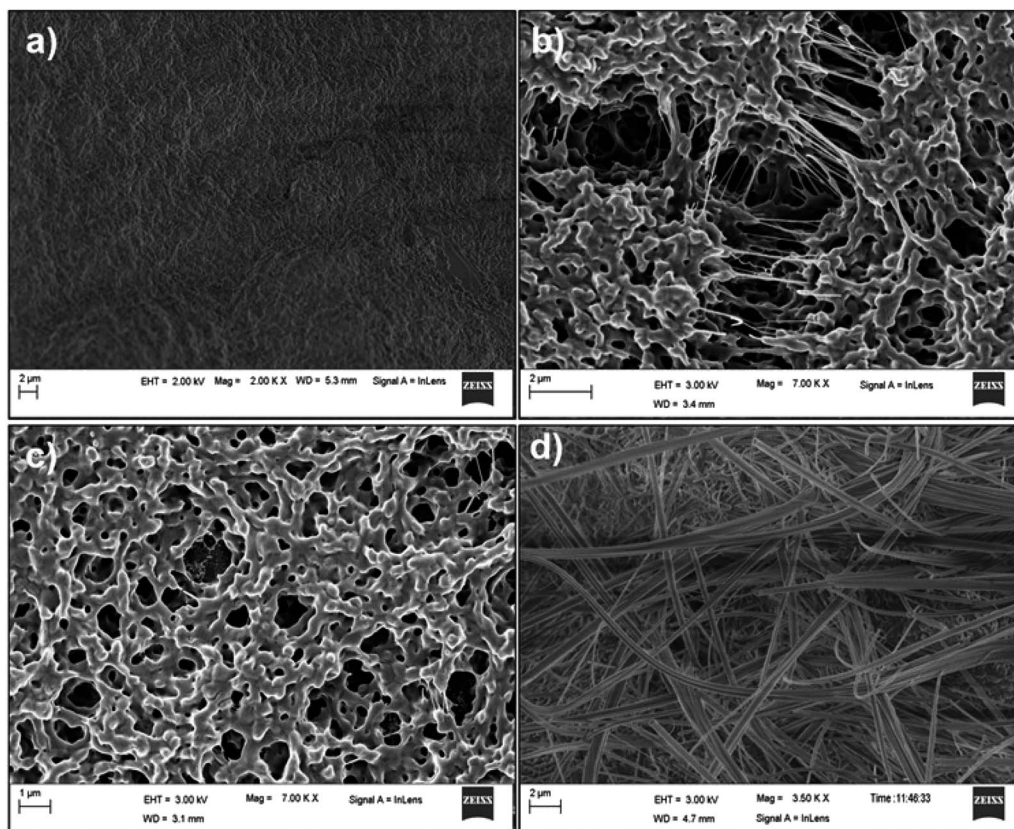


Fig. 2 FESEM images of the organogels obtained in 1,2-DCB for (a) P1, (b) P2, (c) P3 and (d) P4.

studied by rheology. The storage modulus (G') and the loss modulus (G'') were measured as functions of different parameters such as angular frequency and the strain sweep. For this study, gels were formed from **P1–P4** in 1,2-DCB at 1.0% w/v. In the angular frequency sweep experiment that was performed at a constant strain of 0.1% at 25 °C, for all four organogels, the G' value was found to dominate over the G'' value, until about 100 rad s^{-1} (Fig. 3a and S14a†). In addition, G' and G'' were found to be independent of angular frequency in the region of 1–100 rad s^{-1} ,

indicating the formation of stable organogels. The storage moduli of all the organogels were of the order of $\geq 10^4$ Pa in the frequency sweep experiment, indicating considerable mechanical strength of all the organogels. In the strain sweep experiment, where the storage moduli (G') and the loss moduli (G'') for the four organogels were plotted as a function of % strain (0.1–100%) (Fig. 3b and S14b†), it was found that G' was higher than G'' (of the order of 10^4 Pa) until a particular strain (linear viscoelastic region (LVR), $\gamma = 0.1\%$ for **P1–P4**).

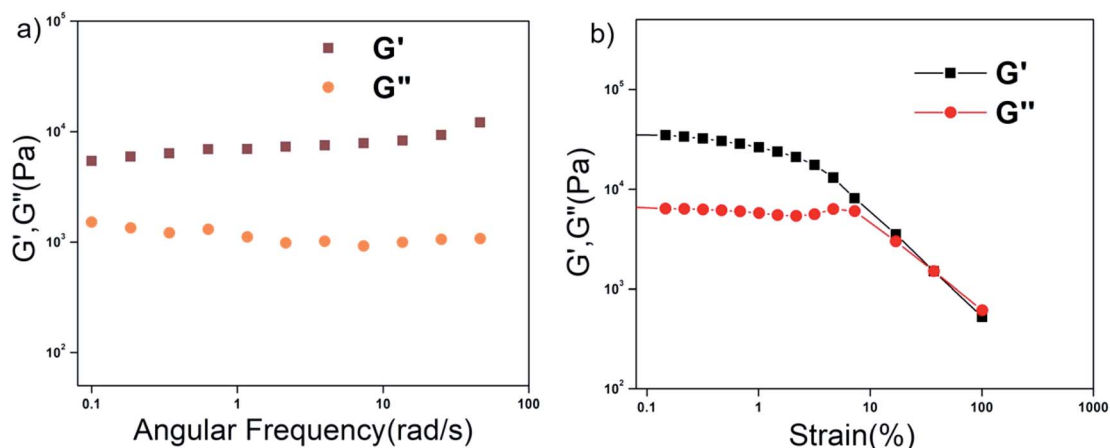


Fig. 3 Rheology of the P1 xerogel. (a) Frequency dependence and (b) strain dependence of the dynamic storage modulus (G') and the loss modulus (G'') of the organogel from P1 in 1,2-DCB at 2% w/v.



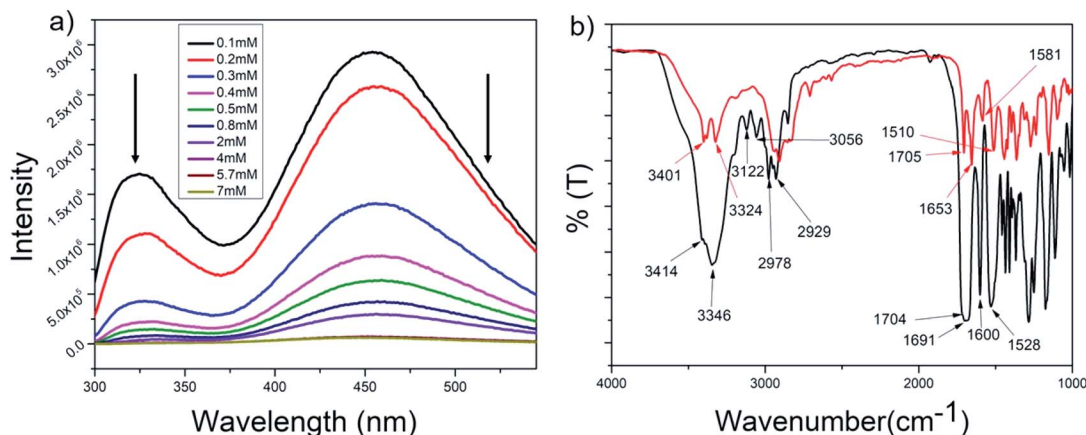


Fig. 4 (a) Concentration dependent tryptophan fluorescence spectra for **P1** in THF (λ_{ex} at 280 nm) and (b) superimposed FTIR spectra of **P1** in the powdered (black) and xerogel (red) states.

Non-covalent interactions in promoting self-assembly

The peptides were designed to be hydrophobic and rich in aromatic moieties. Thus, aromatic π - π interactions and hydrophobic interactions were expected to be the key non-covalent forces driving self-assembly. Peptide backbones are rich in hydrogen bond donor and acceptor groups and hence hydrogen bonding might be another important factor aiding self-assembly. The following experiments were performed to identify the key interactions driving the assembly process.

Fluorescence studies

The intrinsic fluorescence of the tryptophan residue was used to study the role of aromatic π - π stacking interactions in the self-assembly of peptide **P1**. Fig. 4a shows the fluorescence emission spectra of **P1** in THF at various concentrations (0.1–7 mM). The emission maxima of tryptophan at 325 nm was steadily quenched upon increasing the concentration of the peptide. This could be attributed to the stacking of the tryptophan moieties with progressive self-assembly upon increasing the concentration of the peptide. A prominent excimer peak was observed at 455 nm, and this was quenched upon increasing the concentration of the peptide. Usually, increasing the peptide concentration leads to more excimer formation, which is accompanied by an increase in the intensity of the excimer fluorescence peak. **P1** contains two types of aromatic moieties, the indole ring from Trp and the aromatic backbone of the PABA amino acid. If the self-assembly of **P1** leads to stacking of these two different moieties, then an exciplex is formed instead of an excimer. The fluorescence intensity for the exciplex may be quenched with the increase in the concentration of the exciplex.¹⁰¹ Thus, this experiment clearly proves that in the case of **P1**, aromatic π - π stacking interactions play an important role and suggests that stacking occurs between the Trp side chains and the aromatic ring of PABA.

As peptides **P2–P4** are structurally very similar to **P1**, it can be assumed that aromatic stacking also plays an important role in their self-assembly.

FT-IR

Fig. 4b shows the superposition of the FT-IR spectra recorded for the powder and xerogel samples in 1,2-DCB for **P1**. There are two distinct peaks observed at 3414 and 3346 cm^{-1} in the powdered form of **P1** for non-hydrogen bonded and hydrogen bonded NHs, respectively, and these shift to 3401 and 3324 cm^{-1} , respectively, in the xerogel, indicating increased hydrogen bonding in the xerogel state. However, the presence of two peaks indicates both the existence of hydrogen bonded and non-hydrogen bonded NHs. The CO stretching frequency shifts from 1691 cm^{-1} in the powdered form to 1653 cm^{-1} in the xerogel form, suggesting that the backbone conformation of the **P1** is not beta sheet-like. In the case of **P2–P4** (Fig. 5a and S15[†]), a broad peak is observed in the NH stretching region at around 3420–3430 cm^{-1} for the xerogel, indicating the presence of non-hydrogen bonded backbone NHs. The lack of any peak at around 3200 cm^{-1} suggests the absence of hydrogen bonded amide protons in these systems in the self-assembled state. The amide I peaks in **P2–P4** do not indicate a typical β -sheet type of conformation. The presence of the hydrogen bonding status of the amide protons was further studied using NMR spectroscopy.

NMR

The role of intermolecular hydrogen bonds in driving self-assembly was probed by monitoring the NH chemical shifts of **P1** and **P2** in CDCl_3 at concentrations below, above and at their minimum gelation concentration (Fig. S16a and b[†]). For both peptides, none of the NH protons showed any change in their chemical shifts over the entire concentration range, indicating that there was no change in the hydrogen bonded state of the backbone amide protons over the concentration range in which the study was performed. Furthermore, in order to understand the hydrogen bonded state of the amide protons, DMSO titration experiments of **P1** and **P2** were performed (Fig. S17[†] and 5b). For **P1**, it was seen that the NH of tryptophan did not show any change in the chemical shift value, suggesting it to be hydrogen bonded, while the NH of the PABA residue and the



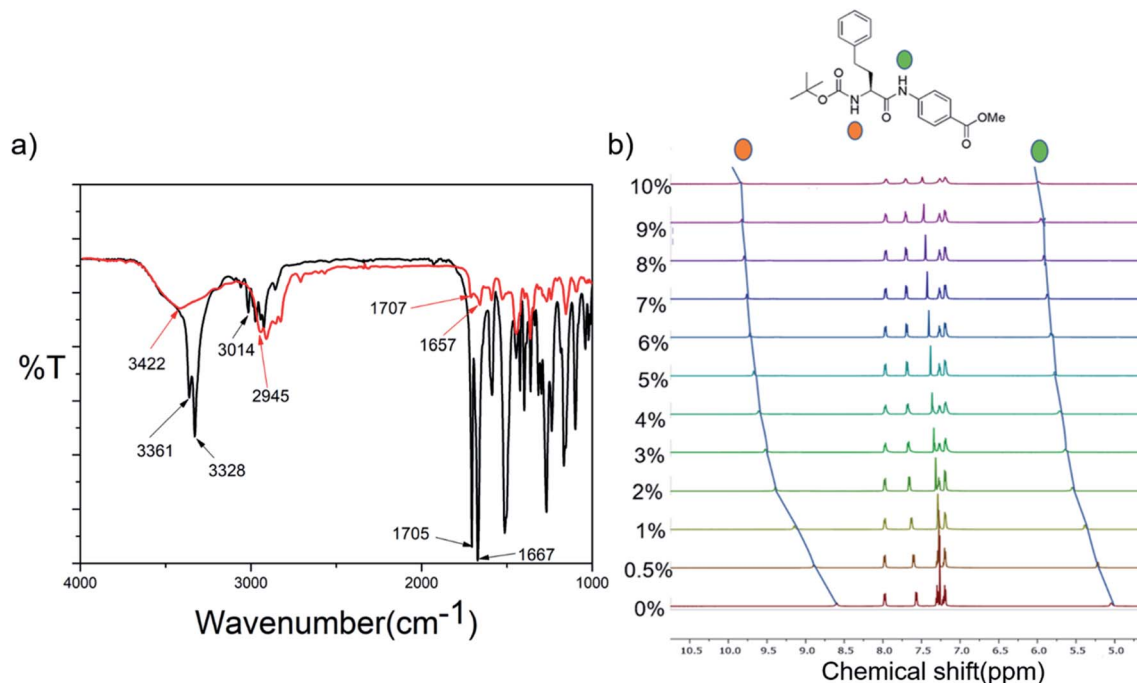


Fig. 5 (a) Superimposed FT-IR spectra of **P2** in powder (black) and xerogel (red) states. (b) Stacked NH region of the ^1H NMR spectra obtained upon addition of increasing amounts of DMSO-d_6 to the CDCl_3 solution of **P2**.

indole NH showed considerable changes in their chemical shift values, suggesting that they were solvent exposed or non-hydrogen bonded. This corroborates the observations from FT-IR experiments of **P1** in the xerogel state, where there was the presence of both hydrogen bonded, as well as non-hydrogen bonded, NHs. Aromatic protons show a striking upfield shift upon the addition of DMSO-d_6 to the CDCl_3 solution of **P1**. The addition of increasing amounts of DMSO-d_6 disrupts the self-assembly, thus changing the electronic environment of the aromatic protons, which become shielded. This is an indirect proof of the fact that stacking of aromatic moieties plays an important role in the self-assembly of **P1**. In the case of **P2**, NHs of both the amino acid residues were solvent exposed or were non-hydrogen bonded, supporting the FT-IR data where only a broad peak corresponding to non-hydrogen bonded NHs was observed.

Thus, in summary, the hydrogen bonding pattern in **P1** is slightly different from that in **P2–P4**. Hydrogen bonding does not seem to play a crucial role in the self-assembly process of **P2–P4**, unlike it does in **P1**.

PXRD

Information on the molecular packing of peptides **P1–P4** in the gel state was obtained upon performing PXRD experiments (Fig. S18†). The PXRD pattern for the **P1** xerogel is ordered, unlike that for its powdered form (Fig. S19†). The wide angle PXRD patterns for the **P1–P4** xerogels showed similar periodic diffraction patterns, indicating the presence of a similar ordered arrangement in all the xerogels. In the peptide xerogels of **P1–P4**, peaks were observed at d values of 6.25 \AA ($2\theta = 14.12$),

5.19 \AA ($2\theta = 17.04$), 4.75 \AA ($2\theta = 18.64$) and 4.10 \AA ($2\theta = 21.60$) (Table S2†). The ideal centroid to centroid distance in the π – π stacked aromatic systems is about 4 \AA . The distance of 4.20 \AA that was present in all the xerogels may be attributed to the distance in between the aromatic moieties of the gelator molecules present in the system. This again indicates that aromatic π – π interactions are crucial for self-assembly, and that they are present in all the xerogel systems. The peak at around 4 \AA is absent in the PXRD pattern of the powdered samples of **P1**, **P3** and **P4**, indicating the lack of aromatic π – π interactions in the powdered form of the peptides.

Crystal structures of **P2** and **P4**

The structures of peptides **P2** and **P4** were elucidated from the single crystal X-ray analysis. Crystals were grown from the $\text{MeOH-H}_2\text{O}$ system by slow evaporation of solvent at room temperature (Table S3†). The backbone of both peptides **P2** and **P4** are kinked at the $\text{C}\alpha$ carbon of the alpha amino acid residue (Fig. 6, S20 and Table S4†). There are no intramolecular hydrogen bonds present in either of the peptides. We could not obtain crystals for peptides **P1** or **P3** but, as the backbone of all the molecules is the same, we can assume that a similar backbone conformation is also present in **P1** and **P3**. **P2** and **P4** do not have a beta sheet-like conformation, and this explains the absence of any characteristic peak in the amide I region in the FTIR spectra of the xerogels. Fig. S21 and S22† show the packing in crystals of **P2** and **P4**, respectively. The packing in both the systems is fairly similar. For both the peptides, pairs of molecules pack together and such pairs stack to form column-like structures. In the case of **P2**, Boc groups of the two individual



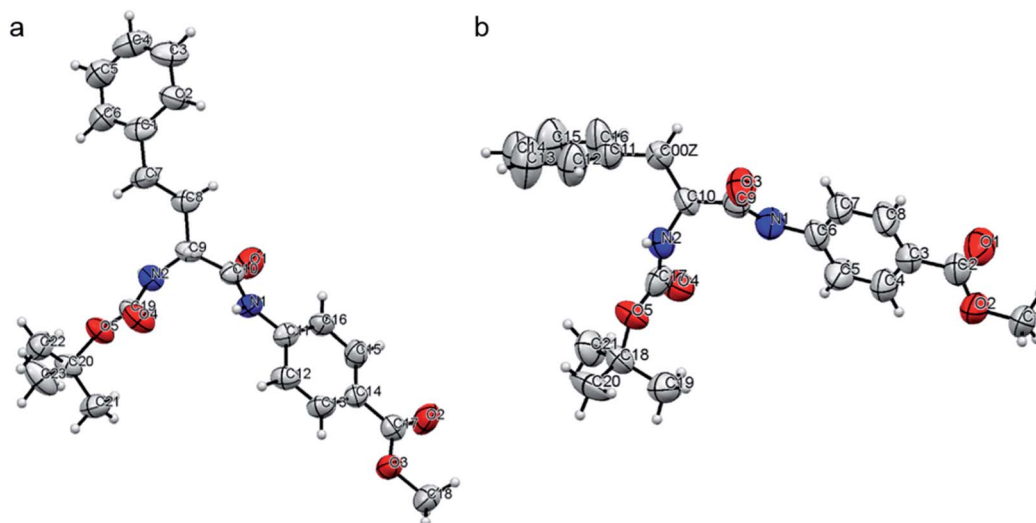


Fig. 6 An ORTEP diagram for peptides (a) **P2** and (b) **P4**, with an ellipsoid of 50% probability, as obtained in the crystals grown from the slow evaporation of MeOH–H₂O.

molecules in a pair face each other. The aromatic rings of PABA come close together, while the aromatic groups of Homo-Phe stick out in opposite directions. In **P4**, the packing of a pair of molecules is a bit different, with the Boc groups of one molecule pointing away from the other and the Phe side chain of one molecule stacking with the phenyl ring in the backbone of PABA of the other molecule. In both **P2** and **P4**, pairs of molecules self-assemble to form columnar structures, primarily through aromatic stacking interactions, hydrophobic interactions and weak hydrogen bonding interactions (C=O...H–N bond distance of about 2.2 Å, Table S5†).

Mechanism of self-assembly

Fig. 7 summarizes the mechanism of self-assembly of LMWG **P1–P4**. The molecules assemble primarily through aromatic pi–pi stacking and hydrophobic interactions. Pi–pi stacking might occur in between the same or different aromatic moieties. Although all the molecules contain ample hydrogen bond donors and acceptors in the backbone, there seems to be an absence of hydrogen bonding in the self-assembled system, as evidenced from the FT-IR and NMR studies. While **P2–P4** completely lack hydrogen bonding, **P1** contains both hydrogen

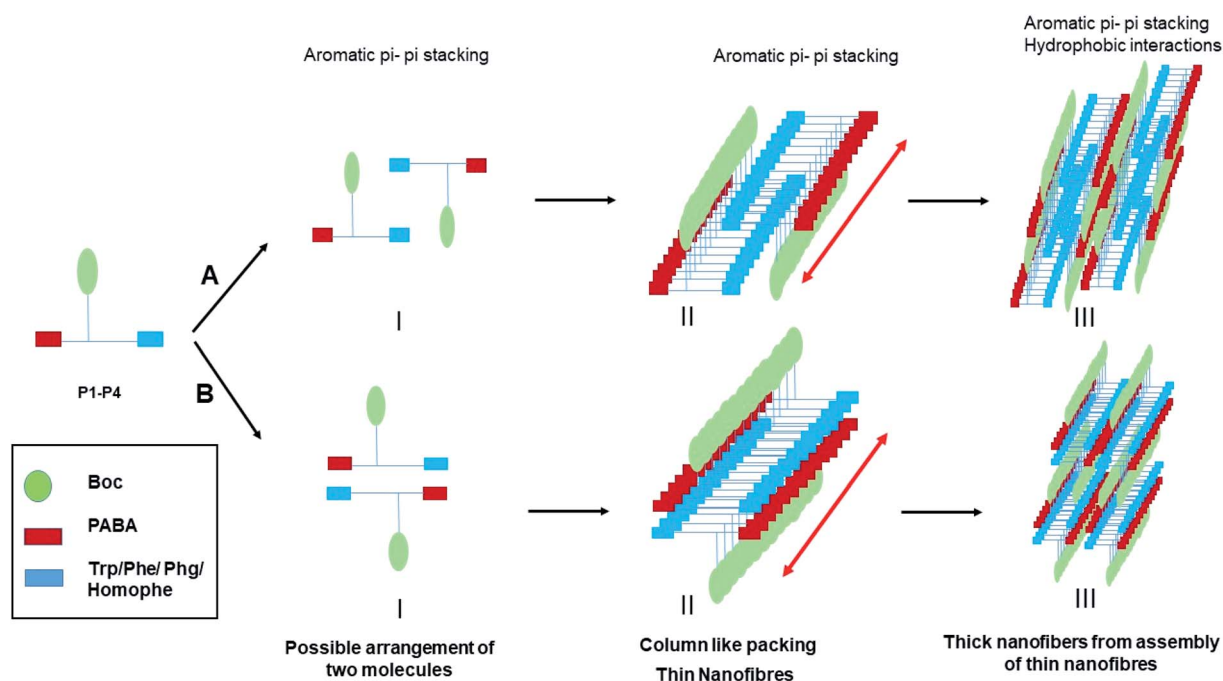


Fig. 7 Mechanism of the self-assembly of **P1–P4**.

bonded and non-hydrogen bonded NHs. In the crystals of **P2** and **P4**, weak hydrogen bonds (2.2 Å) are present, which help with crystal packing. A closer approach of the molecules to yield stronger hydrogen bonding might be absent in the crystals to minimize associated unfavorable van der Waals interactions. In the supramolecular packing arrangement in the organogels, the presence of solvent molecules further weakens the hydrogen bonds to the limit of non-existence. Thus, it is clear that the mere presence of hydrogen bonding groups does not ensure hydrogen bonding to be one of the driving forces in the self-assembly of the system. Instead, the assembly of molecules exploits only those parameters that are sufficient, to give rise to a thermodynamically favored system. In this case, the aromatic pi-pi stacking interactions and the hydrophobic interactions were sufficient enough to create and sustain thermodynamically favorable self-assembly. There might be subtle differences in the self-assembly of the molecules of **P1-P4**, depending on the side chains of the first amino acid residue. However, the global arrangement of the molecules is similar, as evidenced from the PXRD experiments. The backbone conformation of the peptides is kinked at the C α carbon atom, preventing the formation of beta sheets, as is evidenced by the FT-IR studies. The molecules stack on top of each other, initiating unidirectional self-assembly, giving rise to column like structures with fibrous morphology. Many of these thin fibers assemble together due to favorable hydrophobic interactions, forming thicker fibers that are seen in the FESEM experiments.

Careful observation indicates that **P1-P4** form gels in several less polar organic solvents such as in toluene, chloroform,

dichlorobenzene *etc.*, in contrast to more polar organic solvents such as ethanol, DMSO *etc.* This seems to be logical, as the non-polar solvents are better accommodated in the entangled network formed by the hydrophobic peptides **P1-P4**. As the solvents are non-polar and there is no evidence of hydrogen bonding obtained from either FTIR or NMR, it can be concluded that the only interaction of the peptides with the solvents is of hydrophobic origin.

Oil spill recovery

Peptides **P1-P4** phase selectively formed gels in fuels such as kerosene, petrol and diesel in the presence of acidic, basic and saline aqueous media upon being heated and subsequently cooled (Fig. 8, S23b and Table S6†). The gels had a fibrous morphology, as seen from FESEM results (Fig. 8b) and they were mechanically robust (Fig. 8c). In the frequency sweep experiment, the G' value was greater than the G'' value throughout the entire range of the experiment. G' had a value in the order of 10^4 to 10^5 , and this suggested that the gels were robust in nature (Fig. 8c). The backbone conformation of the peptide in the xerogel state was probed using FT-IR (Fig. 8d). Although the amide I peak in the xerogel of **P1** in kerosene at 1636 cm^{-1} was in the antiparallel beta sheet region, the observation of the peak at 3445 cm^{-1} indicated the presence of non-hydrogen bonded amide protons in the system, and this counters the presence of the beta sheet-like conformation. PXRD of the **P1** xerogel in kerosene showed a similar peak pattern and hence interplanar distances as observed for the xerogels of **P1** obtained from other

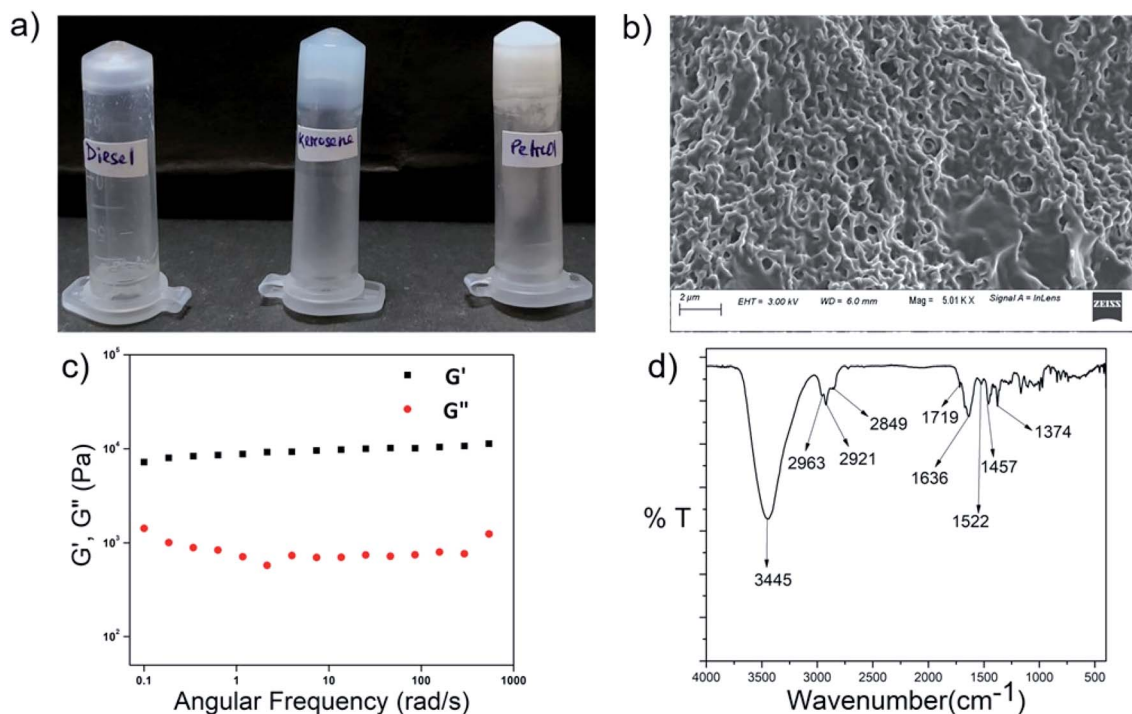


Fig. 8 (a) Gels formed by **P1** in kerosene, diesel and petrol, (b) FESEM image of the **P1** organogel in kerosene, (c) frequency dependence of the dynamic storage modulus (G') and the loss modulus (G'') of the organogel from **P1** in kerosene at 1% w/v. (d) FTIR spectrum of the xerogel of **P1** in kerosene.



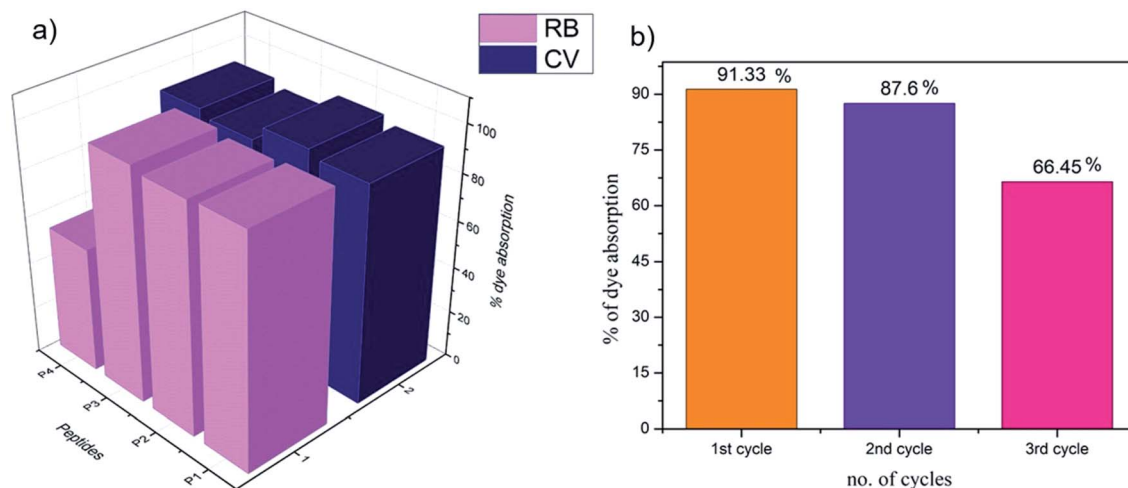


Fig. 9 Dye absorption by the organogels **P1**–**P4** in 1,2-DCB. A bar diagram representing the efficiency of (a) the absorption of cationic dyes CV and RB by organogels **P1**–**P4**, and (b) CV absorption in the subsequent cycles by the organogels from **P1**.

organic solvents (Fig. S23a†). This indicated identical arrangement of the molecules in both cases. Summarizing all of the above, the mode of self-assembly of **P1** in kerosene seems to be identical to that in other organic solvents. About 70% of the kerosene could be easily recovered upon vacuum distillation of the **P1** organogel in kerosene. Facile recovery of the fuel in addition to the gelation ability of the peptides in the presence of variable pH and salt conditions renders the peptides potential candidates for addressing oil spill recovery.

Dye absorption

The presence of organic dye pollutants in water bodies is one of the major concerns for modern civilization. There have been previous reports in the literature on peptide-based dye absorbing materials.^{28–38} The organogels obtained from **P1**–**P4** in the present study were checked for their dye absorption abilities. As the peptides were rich in aromatic moieties and hence rich in electrons, they might be good candidates for the absorption of cationic dyes (Fig. S24 and S25†). Most of the organogels showed high efficiency ($\geq 90\%$) of absorption of the representative cationic dyes CV and RB (Fig. 9a and Table S7†). Organogel **P4** showed relatively less efficiency in the absorption of RB.

Reusability of the organogel for dye absorption

For commercial use as dye absorbents in the purification of water, organogels should be reusable. The dyes could be released in diethyl ether medium over 24 hours and the original organogel recovered. The organogels from **P1**–**P4** were tested for three consecutive cycles. Fig. 9b indicates the decreasing loading capacity of CV by the **P1** organogel in three subsequent cycles.

RGO incorporated organogels

In order to fabricate conducting organogels, we incorporated RGO into organogels from **P1**–**P4**. Reduced graphene oxide is

conducting in nature, unlike graphene oxide. As the peptides **P1**–**P4** were rich in aromatic amino acid residues, the incorporation of RGO into the gel was anticipated to be facilitated by aromatic pi-pi stacking interactions. All the peptides formed organogels in the presence of RGO at their MGC in 1,2-DCB (Fig. 10a). The RGO containing peptide organogels were thermoreversible in nature. The RGO doped organogels were thermostable in nature and their T_{gel} values were in the same range as those of the native gels. Different amounts of RGO were incorporated into the **P1** organogel. In the present study, we incorporated a maximum of 1.2 wt% of RGO into the hybrid gels without destroying the gelation ability of the peptide gelator molecules. Attempts to load higher percentages of RGO in these organogels led to the precipitation of RGO and the formation of inhomogeneous material.

To probe the morphology, FESEM was performed on the **P1**-RGO organogel. Fig. 10b shows the presence of both the RGO nanosheets and the peptide fibers in the hybrid RGO-**P1** organogels containing 1 wt% of RGO. The RGO nanosheets are clearly visible with the peptide fibrous network dispersed on its surface, indicating good interaction in between the components of the hybrid organogel system. As the peptides are hydrophobic and contain a considerable amount of aromatic moieties, a good interaction with the RGO, rich in aromatic components, might be anticipated in the hybrid organogel.

To understand the backbone conformation of the peptide molecules in the hybrid organogel RGO-**P1**, FTIR was performed on the xerogel containing 1 wt% RGO (Fig. S26a†). The NH stretching frequency was observed at 3421 cm^{-1} , indicating the presence of non-hydrogen bonded NHs in the hybrid xerogel, much like in the scenario of the pristine xerogels made from peptides alone. The amide I stretching peak was observed at 1667 cm^{-1} , similar to that obtained from the xerogel containing the peptide alone. Thus, the backbone conformation of the peptides is identical both in the pristine and in the RGO-**P1** xerogel. PXRD data obtained from the RGO-**P1** xerogel is similar to that obtained from the pristine xerogel, indicating that the



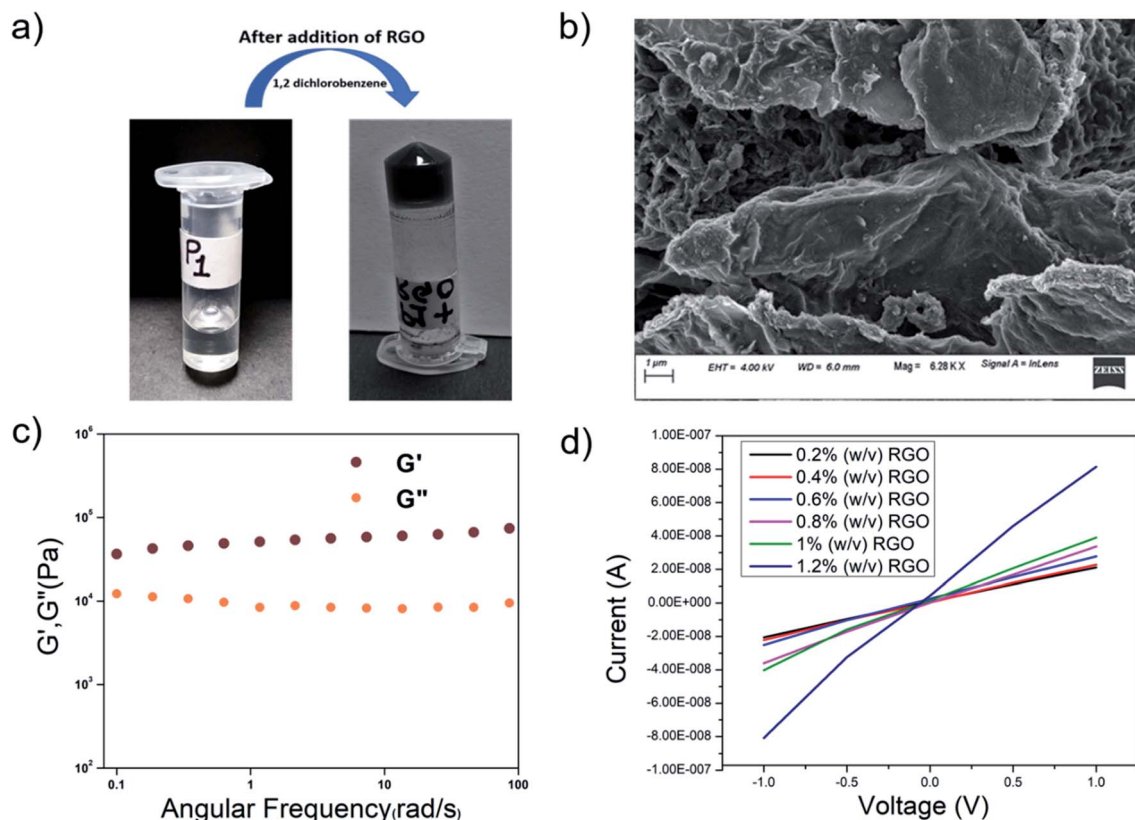


Fig. 10 (a) The reduced graphene oxide incorporated hybrid organogel RGO-P1. (b) An FESEM image of the RGO-P1 hybrid organogel. (c) Frequency dependence of the dynamic storage modulus (G') and the loss modulus (G'') of the RGO-P1 hybrid organogel (1 wt%) in 1,2-DCB. (d) I - V curve showing the conductivity of the hybrid organogels upon RGO incorporation.

solid-state arrangement of the molecules is the same in both the hybrid and in the pristine organogel systems.

The viscoelastic properties of the RGO-P1 xerogel were probed by rheological studies. Studies were performed on the RGO-P1 hybrid organogels containing 1 wt% of RGO (Fig. 10c). In the frequency sweep experiment, the value of G' was greater than that of G'' throughout the experimental limits, indicating that the hybrid organogels were “solid-like”, which is similar to the native gel. Interestingly, the values of G' and G'' increased 10-fold in the case of RGO-P1 containing 1 wt% of RGO, in comparison to the native gel. This means that the incorporation of RGO enhances the rigidity of the gel. This could be attributed to the favorable interaction between the peptide nanofibers and the RGO sheets.

In summary, the insertion of RGO into the peptide organogel did not disrupt the self-assembly pattern that was present in the peptide-only system. The backbone conformation, solid-state packing *etc.* remained unaltered upon insertion of RGO. From the FESEM images, it was evident that both RGO and the peptides retained their distinct morphologies. Hence, the mode of co-assembly may be considered as “orthogonal” in this case. Favorable aromatic interactions between the peptides and the RGO might result in increased rigidity in the system.

Graphene is known for its highly conducting nature. The oxidation of graphite to graphene oxide changes some carbons

to sp^3 , thus destroying the conductivity of the material. RGO, on the other hand, once again becomes conducting in nature, though it is not as good as graphene. Upon incorporation of RGO into the organogels, the hybrid materials became conducting in nature. There have been lots of studies in the literature where hybrid materials containing graphene and its derivatives have been used for energy conversion and storage.^{85–89} Most of these hybrid materials are of an inorganic nature and have high conductivity. There are fewer examples of peptide-based materials containing graphene and its derivatives.^{90,91} Although peptide-based hybrid materials are less conducting in nature compared to their inorganic counterparts, they are interesting as they might find applications in biomedical applications/devices, due to their biocompatibility. Fig. 10d shows the I - V curves obtained from the hybrid organogel RGO-P1 containing different amounts of RGO. The conductivity of the RGO-doped organogels increased proportionately to the amount of RGO in them. Homogeneous gels could not be prepared beyond the insertion of 1.2 w/v% of RGO, hence they were not considered for conductivity studies.

Conclusions

Small gelator peptides that are rich in aromatic moieties were designed in this work, and they readily formed phase selective,



thermoreversible, mechanically robust organogels in a large variety of organic solvents and in fuels such as kerosene, diesel and petrol. The phase selective gelation ability of **P1–P4** in petroleum fuels in various pH and saline conditions renders these organogels as potential materials for controlling marine oil spills. Aromatic pi–pi stacking and hydrophobic interactions were the driving forces for the assembly process, while hydrogen bonding played a trivial role in some systems and was completely absent in others. All four organogels, obtained from **P1–P4**, were excellent dye absorbents and are potential materials to be used in water purification. RGO was incorporated into the peptide organogels to yield hybrid organogels that were conducting in nature. The hybrid organogels were more rigid than the native peptide gels and their conductivity was proportional to the RGO content of the organogel. Hence, with rational design of the structural components in the LMWG, self-assembly can be directed to yield materials that are economically viable, recyclable and that can be utilized for multiple applications.

Abbreviations

DCU	Dicyclohexyl urea
Boc	Tertiary butyloxycarbonyl
FESEM	Field emission scanning electron microscopy
NMR	Nuclear magnetic resonance
FTIR	Fourier-transform infrared spectroscopy
PXRD	Powder X-ray diffraction
LMWG	Low molecular weight gelators
1,2 DCB	1,2 Dichlorobenzene
CV	Crystal violet
RB	Rhodamine B
MGC	Minimum gelation concentration
Trp	Tryptophan
Phe	Phenylalanine
Phg	Phenyl glycine
Homo-Phe	Homo phenylalanine
PABA	<i>para</i> aminobenzoic acid
RT	Room temperature
THF	Tetrahydrofuran
CDCl ₃	Chloroform
DMSO-d ₆	Dimethyl sulfoxide
GO	Graphene oxide
RGO	Reduced graphene oxide

Author contributions

S. Chatterjee designed the project, M. C. and S. D. performed most of the experiments. S. C. performed the rheological experiments. S. Chatterjee analyzed the data and wrote the paper.

Conflicts of interest

There are no conflicts to declare.

Acknowledgements

Chatterjee would like to acknowledge the Department of Science and Technology, India (Fast Track Project No. SB/FT/CS-070/2014) for financial support, and the COE FAST File No. 22-3/2016-TS.II/TC for use of the NMR instrument required in this research. S. Chatterjee acknowledges Arindam Bikash Neog for assistance in RGO synthesis. M. C., S. D. and S. C. acknowledge the IIT Guwahati for Scholarship, and the Central Instruments Facility, IITG for use of the FESEM instrument facility.

References

- P. Dastidar, *Chem. Soc. Rev.*, 2008, **37**, 2699.
- N. M. Sangeetha and U. Maitra, *Chem. Soc. Rev.*, 2005, **34**, 821.
- G. Yu, X. Yan, C. Han and F. Huang, *Chem. Soc. Rev.*, 2013, **42**, 6697.
- S. Bera and D. Haldar, *J. Mater. Chem. A*, 2016, **4**, 6933.
- A. Harada, R. Kobayashi, Y. Takashima, A. Hashidzume and H. Yamaguchi, *Nat. Chem.*, 2011, **3**, 34.
- T. Park and S. C. Zimmerman, *J. Am. Chem. Soc.*, 2006, **128**, 11582.
- A. Ajayaghosh and V. K. Praveen, *Acc. Chem. Res.*, 2007, **40**, 644.
- S. Tanaka, M. Shirakawa, K. Kaneko, M. Takeuchi and S. Shinkai, *Langmuir*, 2005, **21**, 2163.
- T. Tu, W. Fang, X. Bao, X. Li and K. H. Dotz, *Angew. Chem., Int. Ed.*, 2011, **50**, 6601.
- N. Fujita, Y. Sakamoto, M. Shirakawa, M. Ojima, A. Fujii, M. Ozaki and S. Shinkai, *J. Am. Chem. Soc.*, 2007, **129**, 4134.
- S. Xiao, Y. Zou, M. Yu, T. Yi, Y. Zhou, F. Li and C. A. Huang, *Chem. Commun.*, 2007, 4758.
- J. J. D. Jong, L. N. Lucas, R. M. Kellogg and J. H. V. Esch, *Science*, 2004, **304**, 278.
- W. Cai, G. T. Wang, Y. X. Xu, K. Jiang and Z. T. Li, *J. Am. Chem. Soc.*, 2008, **130**, 6936.
- O. J. Dautel, M. Robitzer, J. P. L. Porte, F. S. Spirau and J. J. E. Moreau, *J. Am. Chem. Soc.*, 2006, **128**, 16213.
- P. Xue, R. Lu, G. Chen, Y. Zhang, H. Nomoto, M. Takafuji and H. Ihara, *Chem.–Eur. J.*, 2007, **13**, 8231.
- D. Bardelang, *Soft Matter*, 2009, **5**, 1969.
- Y. Li, T. Wang and M. Liu, *Tetrahedron*, 2007, **63**, 7468.
- G. Cravotto and P. Cintas, *Chem. Soc. Rev.*, 2009, **38**, 2684.
- C. Dou, D. Li, H. Gao, C. Wang, H. Zhang and Y. Wang, *Langmuir*, 2010, **26**, 2113.
- T. Naota and H. Koori, *J. Am. Chem. Soc.*, 2005, **127**, 9324.
- K. Isozaki, H. Takaya and T. Naota, *Angew. Chem., Int. Ed.*, 2007, **46**, 2855.
- H. Maeda, *Chem.–Eur. J.*, 2008, **14**, 11274.
- A. Ajayaghosh, P. Chithra and R. Varghese, *Angew. Chem., Int. Ed.*, 2007, **46**, 230.
- H. J. Kim, J. H. Lee and M. Lee, *Angew. Chem., Int. Ed.*, 2005, **44**, 5810.
- K. Basu, N. Nandi, B. Mondal, A. Dehsorkhi, I. W. Hamley and A. Bannerjee, *Interface Focus*, 2017, **7**, 1.



- 26 M. Konda, I. Maity, D. B. Rasale and A. K. Das, *ChemPlusChem*, 2014, **79**, 1482.
- 27 S. Basak, J. Nanda and A. Banerjee, *J. Mater. Chem.*, 2012, **22**, 11658.
- 28 D. M. Wood, B. W. Greenland, A. L. Acton, F. Rodríguez-Llansola, C. A. Murray, C. J. Cardin, J. F. Miravet, B. Escuder, I. W. Hamley and W. Hayes, *Chem.-Eur. J.*, 2012, **18**, 2692.
- 29 F. Rodríguez-Llansola, B. Escuder, J. F. Miravet, D. Hermida-Merino, I. W. Hamley, C. J. Cardin and W. Hayes, *Chem. Commun.*, 2010, **46**, 7960.
- 30 S. Basak, N. Nandi, S. Paul, I. W. Hamley and A. Banerjee, *Chem. Commun.*, 2017, **53**, 5910.
- 31 B. Adhikari, G. Palui and A. Banerjee, *Soft Matter*, 2009, **5**, 3452.
- 32 S. Ray, A. K. Das and A. Banerjee, *Chem. Mater.*, 2007, **19**, 1633.
- 33 B. O. Okesola and D. K. Smith, *Chem. Commun.*, 2013, **49**, 11164.
- 34 P. Chakraborty, B. Roy, P. Bairi and A. K. Nandi, *J. Mater. Chem.*, 2012, **22**, 20291.
- 35 S. Sengupta and R. Mondal, *J. Mater. Chem. A*, 2014, **2**, 16373.
- 36 A. Chakrabarty, U. Maitra and A. D. Das, *J. Mater. Chem.*, 2012, **22**, 18268.
- 37 N. Cheng, Q. Hu, Y. Guo, Y. Wang and L. Yu, *ACS Appl. Mater. Interfaces*, 2015, **7**, 10258.
- 38 S. Debnath, A. Shome, S. Dutta S and P. K. Das, *Chem.-Eur. J.*, 2008, **14**, 6870.
- 39 J. H. Jung, H. Kobayashi, M. Masuda, T. Shimizu and S. Shinkai, *J. Am. Chem. Soc.*, 2001, **123**, 8785.
- 40 E. D. Sone, E. R. Zubarev and S. I. Stupp, *Angew. Chem., Int. Ed.*, 2002, **41**, 1705.
- 41 S. Kobayashi, N. Hamasaki, M. Suzuki, M. Kimura, H. Shinkai and K. Hanabusa, *J. Am. Chem. Soc.*, 2002, **124**, 6550.
- 42 C. Zhan, J. Wang, J. Yuan, H. Gong, Y. Liu and M. Liu, *Langmuir*, 2003, **19**, 9440.
- 43 S. Kobayashi, K. Hanabusa, N. Hamasaki, M. Kimura, H. Shirai and S. Shinkai, *Chem. Mater.*, 2000, **12**, 1523.
- 44 P. Xue, R. Lu, Y. Huang, M. Jin, C. Tan, C. Bao, Z. Wang and Y. Zhao, *Langmuir*, 2004, **20**, 6470.
- 45 M. Tena-Solsona, J. Nanda, S. Díaz-Oltra, A. Chotera, G. Ashkenasy and B. Escuder, *Chem.-Eur. J.*, 2016, **22**, 6687.
- 46 B. Escuder, F. Rodríguez-Llansola and J. F. Miravet, *New J. Chem.*, 2010, **34**, 1044.
- 47 W. Kubo, T. Kitamura, K. Hanabusa, Y. Wada and S. Yanagida, *Chem. Commun.*, 2002, 374.
- 48 Y. Yamada and J. P. Schneider, *Biomacromolecules*, 2016, **17**, 2634.
- 49 S. R. Jadhav, B. S. Chiou, D. F. Wood, G. DeGrande Hoffman, G. M. Glenn and G. John, *Soft Matter*, 2011, **7**, 864.
- 50 K. Basu, A. Baral, S. Basak, A. Dehsorkhi, J. Nanda, D. Bhunia, S. Ghosh, V. Castelletto, I. W. Hamley and A. Banerjee, *Chem. Commun.*, 2016, **52**, 5045.
- 51 J. E. P. Sun, B. Stewart, A. Litan, S. J. Lee, J. P. Schneider, S. A. Langhans and D. J. Pochan, *Biomater. Sci.*, 2016, **4**, 839.
- 52 V. Castelletto, A. Kaur, I. W. Hamley, R. H. Barnes, K. A. Karatzas, D. Hermida-Merino, S. Swioklo, C. J. Connon, J. Stasiak, M. Reza and J. Ruokolainen, *RSC Adv.*, 2017, **7**, 8366.
- 53 S. Ray, A. K. Das and A. Banerjee, *Chem. Mater.*, 2007, **19**, 1633.
- 54 J. Nanda and A. Banerjee, *Soft Matter*, 2012, **8**, 3380.
- 55 M. Schroppe, *Nature*, 2011, **472**, 152.
- 56 B. Wang, W. Liang, Z. Guo and W. Liub, *Chem. Soc. Rev.*, 2015, **44**, 336.
- 57 S. Venkatanarasimhan and D. Raghavachari, *J. Mater. Chem. A*, 2013, **1**, 868.
- 58 R. J. Fiocco and A. Lewis, *Pure Appl. Chem.*, 1999, **71**, 27.
- 59 E. Pelletier and R. Siron, *Environ. Toxicol. Chem.*, 1999, **18**, 813.
- 60 F. L. Motta, S. R. Stoyanov and J. B. P. Soares, *Chemosphere*, 2018, **194**, 837.
- 61 D. Sundaravadivelu, M. T. Suidan, A. D. Venosa and P. I. Rosales, *Chemosphere*, 2016, **144**, 1490.
- 62 A. Tripathi, G. N. Parsons, O. J. Rojas and S. A. Khan, *ACS Omega*, 2017, **2**, 4297.
- 63 H. M. Choi, *Environ. Sci. Technol.*, 1992, **26**, 772.
- 64 V. Singh, S. Jinka, K. Hake, S. Parameswaran, R. J. Kendall and S. Ramkumar, *Ind. Eng. Chem. Res.*, 2014, **53**, 11954.
- 65 N. Widiaksana, A. A. Yudianta and Y. S. Nugroho, *IOP Conf. Ser. Earth Environ. Sci.*, 2018, **105**, 1755.
- 66 S. Khandakar, M. N. Islam, R. I. Rubel and S. S. Yusuf, *Bitlis Eren Univ. J. Sci. Technol.*, 2017, **7**, 115.
- 67 A. T. Hoang, V. V. Pham and D. N. Nguyen, *Int. J. Appl. Eng. Res.*, 2018, **13**, 4915.
- 68 S. Mondal, P. Bairi, S. Das and A. K. Nandi, *J. Mater. Chem. A*, 2019, **7**, 381.
- 69 S. Bhattacharya and Y. Krishnan-Ghosh, *Chem. Commun.*, 2001, 185.
- 70 M. Konda, I. Maity, D. B. Rasale and A. K. Das, *ChemPlusChem*, 2014, **79**, 1482.
- 71 K. Basu, N. Nandi, B. Mondal, A. Dehsorkhi, I. W. Hamley and A. Banerjee, *Interface Focus*, 2017, **7**, 1.
- 72 N. D. Lourenco, J. M. Novais and H. M. Pinheiro, *J. Biotechnol.*, 2001, **89**, 163.
- 73 A. H. Gemeay, I. A. Mansour, R. G. El-Sharkawy and A. B. Zaki, *J. Mol. Catal. A: Chem.*, 2003, **193**, 109.
- 74 N. Daneshvar, H. Ashassi-Sorkhabi and A. Tizpar, *Sep. Purif. Technol.*, 2003, **31**, 153.
- 75 E. Rindle and W. J. Troll, *J. Natl. Cancer Inst.*, 1975, **55**, 181.
- 76 D. Solpan and O. Guven, *Radiat. Phys. Chem.*, 2002, **65**, 549.
- 77 S. Kalyuzhnyi and V. Sklyar, *Water Sci. Technol.*, 2000, **12**, 23.
- 78 F. I. Hai, K. Yamamoto and K. Fukushima, *Crit. Rev. Environ. Sci. Technol.*, 2007, **37**, 315.
- 79 E. K. Schillinger, E. Mena-Osteritz, J. Hentschel, H. G. Börner and P. Bäuerle, *Adv. Mater.*, 2009, **21**, 1562.
- 80 E. Jahnke, J. Weiss, S. Neuhaus, T. N. Hoheisel and H. Frauenrath, *Chem.-Eur. J.*, 2009, **15**, 388.
- 81 S. Bai, S. Debnath, N. Javid, P. W. J. M. Frederix, S. Fleming, C. Pappas and R. V. Ulijn, *Langmuir*, 2014, **30**, 7576.



- 82 H. Xu, A. K. Das, M. Horie, M. S. Shaik, A. M. Smith, Y. Luo, X. Lu, R. Collins, S. Y. Liem, A. Song, P. L. A. Popelier, M. L. Turner, P. Xiao, I. A. Kinloch and R. V. Ulijn, *Nanoscale*, 2010, **2**, 960.
- 83 E. Torres, J. Puigmarti-Luis, A. Perez del Pino, R. M. Ortuno and D. B. Amabilino, *Org. Biomol. Chem.*, 2010, **8**, 1661.
- 84 S. K. M. Nalluri, N. Shivarova, A. L. Kanibolotsky, M. Zelzer, S. Gupta, P. W. J. M. Frederix, P. J. Skabara, H. Gleskova and R. V. Ulijn, *Langmuir*, 2014, **30**, 12429.
- 85 X. Huang, X. Qi, F. Boey and H. Zhang, *Chem. Soc. Rev.*, 2012, **41**, 666.
- 86 U. N. Maiti, J. Lim, K. E. Lee, W. J. Lee and S. O. Kim, *Adv. Mater.*, 2014, **26**, 615.
- 87 C. Yang, Z. Liu, C. Chen, K. Shi, L. Zhang, X.-J. Ju, W. Wang, R. Xie and L.-Y. Chu, *ACS Appl. Mater. Interfaces*, 2017, **9**, 15758.
- 88 R. Kumar, R. K. Singh, A. V. Alaferdov and S. A. Moshkalev, *Electrochim. Acta*, 2018, **281**, 78e87.
- 89 R. Kumar, E. T. S. G. da Silva, R. K. Singh, R. Savu, A. V. Alaferdov, L. C. Fonseca, L. C. Carossi, A. Singh, S. Khandka, K. K. Kar, O. L. Alves, L. T. Kubota and S. A. Moshkalev, *J. Colloid Interface Sci.*, 2018, **515**, 160.
- 90 R. Kumar, R. K. Singh, D. P. Singh, A. R. Vaz, R. R. Yadav, C. S. Rout and S. A. Moshkalev, *Mater. Des.*, 2017, **122**, 110.
- 91 R. Kumar, S. Sahoo, E. Joanni, R. K. Singh, W. K. Tan, K. K. Kar and A. Matsuda, *Prog. Energy Combust. Sci.*, 2019, **75**, 100786.
- 92 R. Kumara, E. Joanni, R. K. Singh, D. P. Singh and S. A. Moshkalev, *Prog. Energy Combust. Sci.*, 2018, **67**, 115.
- 93 B. Vedhanarayanan, B. Babu, M. M. Shaijumon and A. Ajayaghosh, *ACS Appl. Mater. Interfaces*, 2017, **9**, 19417.
- 94 R. Y. Kuwahara, T. Oi, K. Hashimoto, S. Tamesue, T. Yamauchi and N. Tsubokawa, *Colloid Polym. Sci.*, 2015, **293**, 1635.
- 95 B. Adhikari, A. Biswas and A. Banerjee, *ACS Appl. Mater. Interfaces*, 2012, **4**, 5472.
- 96 R. Kumar, W. C. Macedo Jr, R. K. Singh, V. S. Tiwari, C. J. L. Constantino, A. Matsuda and S. A. Moshkalev, *ACS Appl. Nano Mater.*, 2019, **2**, 4626.
- 97 B. Adhikari, J. Nanda and A. Banerjee, *Chem.–Eur. J.*, 2011, **17**, 11488.
- 98 B. Adhikari and A. Banerjee, *Soft Matter*, 2011, **7**, 9259.
- 99 T. H. Han, W. J. Lee, D. H. Lee, J. E. Kim, E.-Y. Choi and S. O. Kim, *Adv. Mater.*, 2010, **22**, 2060.
- 100 S. Roy, A. Baral and A. Banerjee, *Chem.–Eur. J.*, 2013, **19**, 14950.
- 101 J. X. Liang, Q. L. Nguyen and S. Matsika, *Photochem. Photobiol. Sci.*, 2013, **12**, 1387.

